Rapid Communications

Broken mirror symmetry tuned topological transport in PbTe/SnTe heterostructures

Feng Wei,[1,2] Chieh-Wen Liu,[3] Da Li,[1] Chun-Yang Wang,[1,2] Hong-Rui Zhang,[2,4] Ji-Rong Sun,[4] Xuan P. A. Gao,[3,*] Song Ma,[1,†] and Zhidong Zhang[1]

[1]*Shenyang National Laboratory for Materials Science, Institute of Metal Research, Chinese Academy of Sciences, 72 Wenhua Road, Shenyang 110016, China*

[2]*University of Chinese Academy of Sciences, Beijing 100049, China*

[3]*Department of Physics, Case Western Reserve University, 2076 Adelbert Road, Cleveland, Ohio 44106, USA*

[4]*Beijing National Laboratory for Condensed Matter Physics, Institute of Physics, Chinese Academy of Sciences, Beijing 100190, China*

(Received 7 May 2018; published 9 October 2018)

The tunability of topological surface states and the controllable opening of the Dirac gap are two keys for the study of topological crystalline insulators (TCIs). By constructing PbTe/SnTe heterostructures, we discover giant linear magnetoresistance (GLMR) (2150% under a magnetic field of 14 T at 2 K) and strong metallic behavior that are likely induced by Dirac fermions with a high carrier mobility. By decreasing the hole density in SnTe, a much weaker metallic behavior and two-dimensional weak antilocalization are exhibited in PbTe/SnTe heterostructures. This striking transport difference is attributed to the cubic-rhombohedral structural phase transition in SnTe and broken mirror symmetry effect. The revelation of lattice structural distortion and mirror symmetry breaking in a PbTe/SnTe heterostructure's transport properties is very significant to the fundamental research in topological matter, magnetoelectronics, and spintronics.

DOI: 10.1103/PhysRevB.98.161301

Topological crystalline insulators (TCIs) are a new topological phase of matter whose topological invariant and conducting boundary states originate from the crystal lattice symmetry [1–4] instead of the time-reversal symmetry of topological insulators (TIs) [5–8]. Unlike conventional Z_2 TIs with a layered structure [9], the TCIs have a rocksalt crystal structure and possess an even number of Dirac cones of topological surface states (TSSs) [3,4], resulting in the possibility of strong coupling with other materials through large proximity effects. Heterointerfacing TIs and band insulators (BIs) can induce diverse new phases such as Dirac semimetals and Weyl semimetals [10–12]. Compared with TIs, the rich interplay between topology, crystal symmetry, and electronic structure in TCIs [13,14] makes it possible to observe novel topological states in the heterointerfaces of TCIs and BIs and exotic physical phenomena such as interface superconductivity [15] and a large-Chern-number quantum anomalous Hall effect [16].

The narrow gap semiconductor SnTe with a rocksalt structure was the first theoretically predicted TCI and its TSS was expected to exist on highly symmetrical crystal surfaces such as {001}, {110}, and {111} [2]. Subsequently, the presence of mirror symmetry protected TSSs in SnTe was verified by angle-resolved photoemission spectroscopy (ARPES) experiments [1]. Motivated by the promising applications of TCIs in low-power electronics and tunable spintronics devices [17], magnetotransport experiments probing the TSSs have been conducted. For example, the weak antilocalization (WAL) effect [18–22] and two-dimensional (2D) Shubnikov–de Haas (SdH) oscillations [20] related to the TSSs were detected in SnTe thin films. The Aharonov-Bohm (AB) effect [21] and high-field linear magnetoresistance (LMR) were observed in low-dimensional SnTe nanostructures [22]. Recently, the lattice distortion and mirror symmetry breaking induced Dirac gap opening in TCIs $Pb_{1-x}Sn_xSe$ was revealed by scanning tunneling microscopy (STM) [13,23] and ARPES [24,25], as theoretically expected [14]. It was established a long time ago that the resistance versus temperature curve $R(T)$ of low doped SnTe shows an anomalous increase near the cubic-rhombohedral structural phase transition temperature [26,27], as a result of the electron-transverse optical (TO)-phonon interaction. After the discovery of the mirror symmetry protected topological properties of SnTe, further addressing the effect of lattice distortion on the TSS transport in SnTe appears to be an interesting and imperative issue.

In this Rapid Communication, we present a systematic investigation on the magnetotransport behavior of the PbTe/SnTe heterostructures grown on $SrTiO_3(111)$ in which the cubic-rhombohedral structural phase transition of SnTe was controlled by the growth condition of the heterostructure. A giant LMR (GLMR) was observed in PbTe/SnTe heterostructures with a high carrier concentration, in which the structural transition is absent. In PbTe/SnTe heterostructures with a reduced carrier density and an anomalous increase in $R_s(T)$, indicative of the cubic-rhombohedral phase transition, 2D WAL is exhibited. Such a remarkable transport difference is likely related to the mirror symmetry breaking in the ⟨110⟩ direction of the SnTe lattice [14].

Epitaxial PbTe/SnTe heterostructures [the inset of Fig. 1(a)] were grown on a $SrTiO_3(111)$ substrate by

*xuan.gao@case.edu
†songma@imr.ac.cn

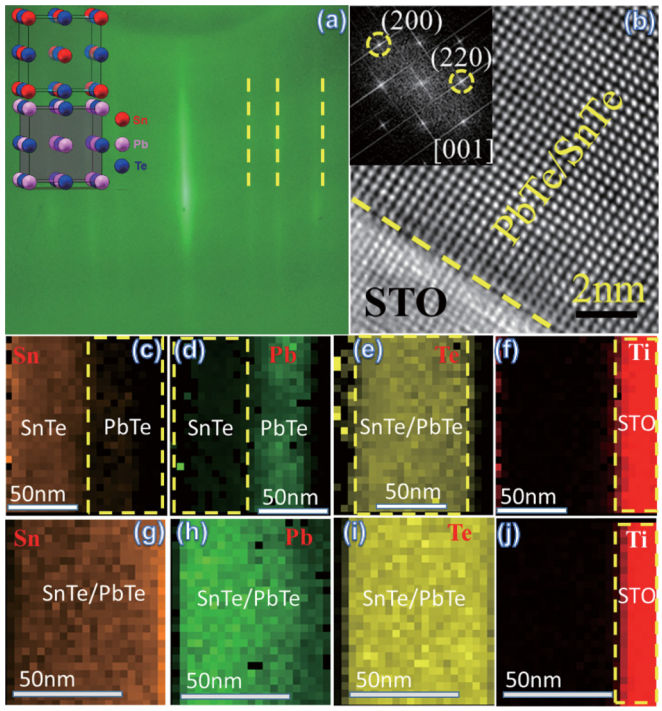

FIG. 1. Structural characterization of PbTe/SnTe heterostructures. (a) RHEED pattern of a PbTe/SnTe heterostructure with a sharp streak. The inset shows the structural schematic of a PbTe/SnTe heterostructure. (b) High-resolution transmission electron microscopy (HRTEM) of a PbTe/SnTe sample and the Fourier transformation of (b) are shown in the inset. (c)–(f) The element mapping for a PbTe/SnTe heterostructure with the lower growth temperature showing a sharp interface between PbTe and SnTe. (g)–(j) The element mapping for a PbTe/SnTe heterostructure with a higher growth temperature showing interdiffusion between PbTe and SnTe.

molecular beam epitaxy (MBE) [for details, see SA in the Supplemental Material (SM) [28]]. The sharp reflection high-energy electron diffraction (RHEED) streaky pattern in Fig. 1(a) indicates the high crystalline quality and atomically flat surface of PbTe/SnTe heterostructures. The x-ray diffraction patterns show the growth direction of PbTe and SnTe along [001] (see SM Fig. S1 [28]) and the cross-section lattice image indicates a good crystalline quality of the PbTe/SnTe heterostructure [Fig. 1(b)]. Moreover, the heterostructures with different growing temperatures are distinguished to have a sharp or interdiffused interface, as demonstrated by the element mappings [Figs. 1(c)–1(j)] in the cross-sectional high-angle annular dark-field (HAADF) scanning transmission electron microscopy (STEM) image and the time-of flight secondary mass spectrometry depth profiles of the heterostructures (SM Fig. S2 [28]). Accordingly, the samples are catalogued into two groups and their transport parameters are shown in Supplemental Material Table S1 [28]. At low temperatures (e.g., 2 K), the sheet resistance R_s of samples with a sharp interface (Nos. 1, 2, 4, 7, 8, and 9) is about three orders lower than that of samples with an interdiffused interface (Nos. 3, 5, 6, 10, and 11), although all the samples have comparable sheet resistances at room temperature. Moreover, we found that the growth temperature also strongly affects the hole density of the sample: Samples with a sharp interface have a much higher hole density than that of samples with an interdiffused interface (SM Table S1 [28]).

The temperature dependence of the sheet resistances R_s for PbTe/SnTe heterostructures with sharp and interdiffused interfaces displays an obvious distinction, although they have a similar thickness configuration. As shown in Fig. 2(a), for samples No. 7 and No. 8 with a sharp interface, their $R_s(T)$ shows a two to three orders drop in resistance at $T < 100$ K, giving rise to an extremely low R_s at low T. Such a strong metallic behavior below 100 K reported in the transport of TCIs may be attributed to the strong metallic TSSs. By contrast, samples No. 6 and No. 10 with an interdiffused interface exhibit a much weaker metallic behavior below 100 K. The $R_s(T)$ curves of other samples in the two categories of interfaces (SM Fig. S3 [28]) also suggest similar differences. Furthermore, the $R_s(T)$ curves exhibit an anomalous increase below 100 K for samples with an interdiffused interface [SM Figs. S4(a)–S4(g) [28]], suggesting the presence of a cubic-rhombohedral structural phase transition [26,27,29]. This cubic-rhombohedral structural phase transition controlled by the interface interdiffusion in the present PbTe/SnTe heterostructures could have a close relation with the distinct MR observed, as we will describe next.

The longitudinal magnetoresistance (MR) of a typical sharp interface sample (sample No. 1) presents an interesting MR feature [Fig. 2(b)]. An unsaturated GLMR up to 2150% is first observed in the TCI system under a magnetic field of 14 T at 2 K and the GLMR is very temperature sensitive: It quickly decreases to 311% at 20 K, which indicates its quantum origin. When a perpendicular/parallel magnetic field is applied to the thin film at 6 K, a striking GLMR difference under different magnetic field directions indicates a typical 2D transport feature of the GLMR [Fig. 2(d)]. When the temperature is increased to 70 K, the GLMR disappears and turns into a classic parabolic MR [Fig. 2(e)]. The gradual decrease of GLMR and the disappearance of the 2D feature with increasing temperature are shown in the Supplemental Material (SM Fig. S5 [28]). Similar samples (Nos. 2, 4, 7, 8, and 9) with a sharp PbTe/SnTe interface also exhibit GLMR behavior (SM Fig. S6 [28]).

For a typical interdiffused interface sample (No. 6), its MR presents a different feature [Fig. 2(c)] when compared with the GLMR in samples with a sharp interface. The low-temperature MR of No. 6 has a much smaller value (less than 3% under 14 T, 2 K). A dip feature near zero field and a classic parabolic MR at higher fields are shown in Fig. 2(c), in which the MR dip signifies the weak antilocalization (WAL) effect. The obvious distinction between MR dips under different directional magnetic fields also indicates a typical 2D transport in the present films [SM Fig. S7(c) [28]]. In 2D diffusive transport, the WAL quantum correction to the magnetoconductance can be fitted by the standard Hikami-Larkin-Nagaoka (HLN) equation [30,31] with the fitting parameters of α and l_Φ, where 2α and l_Φ denote the number of conduction channels and phase coherent length, respectively. Figure 2(f) shows the 2D magnetoconductance of sample No. 6 fitted by the HLN equation with fitting parameters $\alpha = 0.46$ and $l_\Phi = 128$ nm at 2 K (details shown in SM Fig. S7 [28]). l_Φ being greater than the thickness of the film confirms the 2D behavior of the WAL.

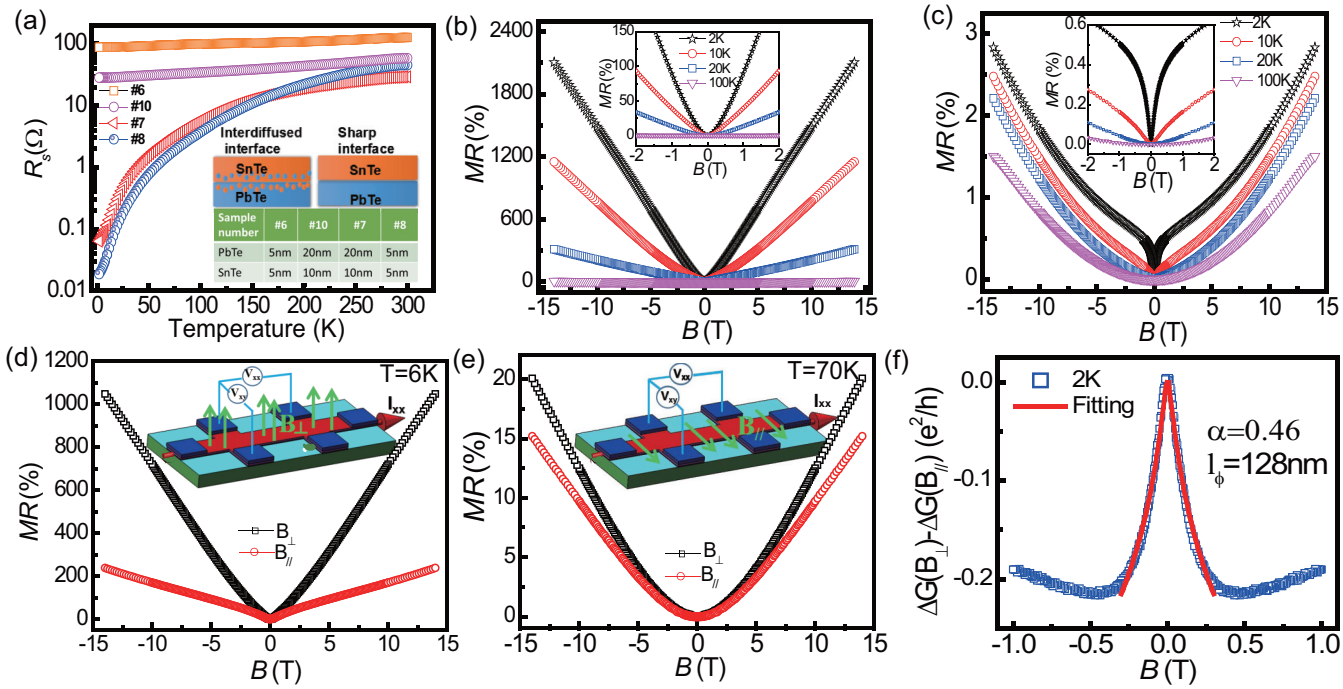

FIG. 2. Two types of temperature and magnetic-field-dependent transport in PbTe/SnTe. (a) Temperature dependence of the sheet resistance R_s (in logarithmic scale) of PbTe/SnTe heterostructures in zero magnetic field. (b) Magnetoresistance (MR) defined as $[R_s(B) - R_s(B=0)]/R_s(B=0)$ at $T = 2-100$ K for a sample with a sharp interface (No. 1) and the zoomed MR curve under low magnetic fields (inset). (c) The MR at $T = 2-100$ K for a sample with an interdiffused interface (No. 6) and the zoomed MR curve under low field (inset). (d), (e) The MR for a sharp interface sample No. 7 at 6 and 70 K under a magnetic field perpendicular/parallel to the plane of the thin film and the measurement schematic shown in the inset. (f) The magnetoconductance fitting of sample No. 6 below 1 T by the HLN equation.

In order to clarify the transport mechanism, the Hall resistances $R_{xy}(B)$ of samples No. 1 and No. 6 at various temperatures are presented in Figs. 3(a) and 3(b). For sample No. 1 with GLMR, a crossover from p-type to n-type carrier dominated conduction was observed around 150–200 K. The

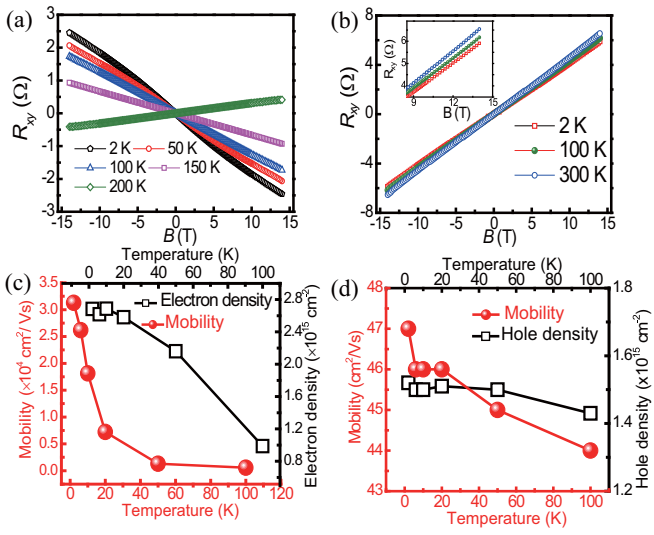

FIG. 3. Temperature dependence of Hall resistance R_{xy} and carrier density/mobility. (a), (b) R_{xy} vs B of (a) sample No. 1 and (b) sample No. 6. (c), (d) Temperature dependence of carrier density and mobility of (c) sample No. 1 and (d) sample No. 6 extracted by fitting the Hall conductance data.

nonlinear Hall curves below 100 K in Fig. 3(a) indicate two carrier types in the transport [32]. According to the two-band model, the nonlinear Hall curve was fitted (SM Fig. S9 [28]) and the carrier density and mobility were obtained as shown in Fig. 3(c). For the samples with GLMR, the n-type carriers exhibit a very high mobility (e.g., reaching 3×10^4 cm^2/V s at 2 K for sample No. 1) below 100 K which is much higher than previously reported SnTe thin films [18–22]. In contrast, sample No. 6 with WAL exhibits p-type conduction in the whole temperature range, suggesting that holes are responsible for the transport of interdiffused PbTe/SnTe heterostructures [Fig. 3(b)]. Because the $R_{xy}(B)$ for sample No. 6 is linear at all temperatures, a single band fitting was used to extract the hole density and mobility as plotted in Fig. 3(d). The nearly-temperature-independent p-type transport, weak metallic $R_s(T)$, and the 2D WAL observed in sample No. 6 are in agreement with many prior works on SnTe films which are known to have dominant p-type behavior from the Sn vacancies in SnTe [18–20].

We now discuss the origin of the different transport behavior in the two types of PbTe/SnTe heterostructures. The sample growth temperature has two direct experimental consequences in the obtained PbTe/SnTe heterostructures. In addition to the effect on sharpness/interdiffusion of the PbTe/SnTe interface shown in Fig. 1, the growth temperature of SnTe also strongly affects the hole density in the SnTe film. Comparing the hole density derived from the Hall data at 150 K for all the samples, we found that the hole density of the samples with interdiffused interfaces is on the order

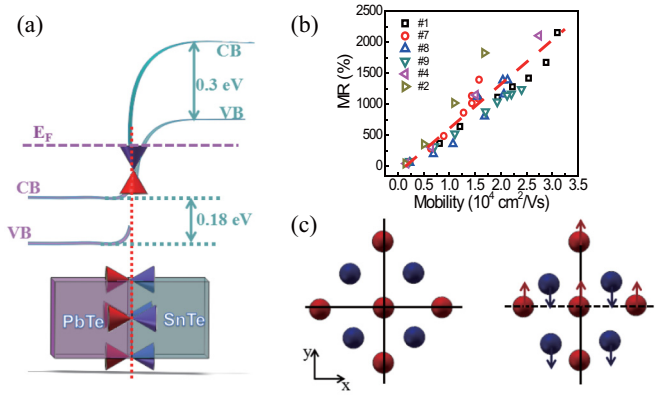

FIG. 4. (a) The band alignment schematic for the PbTe/SnTe heterostructure with a sharp interface. (b) The mobility-dependent MR (%) for samples with GLMR. (c) The schematic lattice change due to the cubic-rhombohedral structural phase transition. The surface mirror line is indicated by solid lines. The dashed line indicates the mirror symmetry breaking due to the distorted SnTe (001) surface. The arrows correspond to the displacement direction of the Sn atom (red) and Te atom (blue).

of $10^{15}/\text{cm}^2$, about one to two orders of magnitude lower than that of the samples with sharp interfaces (SM Table S1 [28]). This trend is consistent with other studies reporting a reduced hole concentration in pure SnTe films grown at higher temperatures [18]. In terms of the volume carrier density, the samples with a sharp interface generally have a hole density $10^{21}-10^{22}/\text{cm}^3$ while the samples with interdiffused interfaces have a hole density $10^{20}-10^{21}/\text{cm}^3$.

The much higher hole density in the PbTe/SnTe samples with sharp interfaces has two main implications. First, it is well known that the PbTe/SnTe heterostructure is of a type-II heterostructure with a broken gap alignment at low temperatures [33,34], where the valence band edge of SnTe is ~0.3 eV higher than the conduction band edge of PbTe at 77 K [33]. Considering the very high hole carrier density ($10^{21}-10^{22}/\text{cm}^3$) in PbTe/SnTe heterostructures with GLMR, the Fermi energy in SnTe is calculated to be 0.36 eV below the valence band (using hole density $10^{21}/\text{cm}^3$ and mass $m^* = m_e$, the free electron mass) which is lower than the Fermi energy of n-type PbTe. Thus the potential equilibration of the Fermi level between PbTe and SnTe leads to electrons transferring from n-type PbTe to p-type SnTe and a downward band bending for the conduction and valence bands of SnTe at the interface, as shown in the band alignment schematic diagram in Fig. 4(a). This downward shift in the energy bands of SnTe also shifts the Dirac point accordingly and causes the Fermi level above the Dirac point at the interface, giving rise to the presence of n-type Dirac electrons in transport at low temperatures. A natural cause for the strong metallic behavior in $R_s(T)$ exhibited below 100 K in samples with sharp interfaces would be the high mobility of the Dirac electrons. In contrast, samples with interdiffused interfaces have a gradual composition change between PbTe and SnTe layers and in such a situation where there is no clear boundary between PbTe and SnTe, the band gap is expected to close/open continuously [33,34] and Dirac surface states are not expected at the interdiffused interface, causing the transport to be dominated by p-type carriers in the SnTe layer throughout the whole temperature range.

Second, the cubic-rhombohedral structural phase transition is known to be dependent on the hole density in SnTe with the transition temperature dropping to zero at a critical hole density around $1.3 \times 10^{21}/\text{cm}^3$ [26]. Note that in this work the highest hole density is $1.38 \times 10^{21}/\text{cm}^3$ in samples with interdiffused interfaces and the minimum hole density of samples with sharp interfaces is $2.35 \times 10^{21}/\text{cm}^3$ (SM Table S1 [28]), placing them below and above the critical density for the cubic-rhombohedral structural phase transition. Indeed, similar to the literature [26,27], we observed a hump feature in the $R_s(T)$ of samples with interdiffused interfaces and low hole densities (SM Fig. S4 [28]), indicating the presence of a structural phase transition but not in the samples with sharp interfaces and high hole densities. The structural phase transition in interdiffused interface samples may cause some interesting effects on the mirror symmetry in the system. As discussed in a theoretical work [14], the displacement between the Sn and Te atoms during the cubic-rhombohedral structural phase transition can break the mirror symmetry along the ⟨110⟩ lattice direction [Fig. 4(c)] and cause the gapping of some Dirac surface states. Therefore, if Dirac surface states exist in interdiffused interface samples (e.g., on the top surface of SnTe), gapping is expected due to the broken mirror symmetry. This effect combined with the disorder/grain boundaries arising from the structural phase transition may be responsible for the low hole mobility shown in interdiffused interface samples [e.g., reaching only 47 $\text{cm}^2/\text{V s}$ at 2 K for No. 6, Fig. 3(d)]. Due to the much lower sheet conductance and lower mobility of interdiffused samples, the WAL quantum correction is relatively big compared to the sample's conductivity and requires a higher magnetic field to suppress (note that the WAL correction to the sheet conductance is on the order of e^2/h and the characteristic magnetic field for WAL is inversely proportional to the square of the phase coherence length). Thus, the 2D WAL is more easily exhibited in the PbTe/SnTe samples with interdiffused interfaces.

Lastly, we like to comment on the GLMR in samples with sharp interfaces. The nonsaturating LMR has always been an intriguing transport phenomenon, and can be a means to detect the band structure of solids [35]. The LMR was first discovered in semimetal Bi with an open Fermi surface [36]. Subsequently, the LMR was revealed in narrow gap semiconductor silver chalcogenides [37]. To explain the physical origin of LMR, Abrikosov's quantum LMR model [38,39] and Parish and Littlewood (PL)'s disorder induced mobility fluctuation model [40,41] were proposed. More recently, LMR has been observed in various Dirac materials with gapless electronic states (e.g., graphene [42], topological insulators [43,44], and Dirac and Weyl semimetals [45,46]). For the GLMR in PbTe/SnTe heterostructures with a sharp interface, the typical 2D feature appears and meanwhile its presence is always accompanied by high mobility. If the present GLMR originates from the mobility fluctuation model in a strongly disordered medium, it would be surprising to see the absolute magnetoresistance increase being much greater than the Hall resistance and the carrier mobility being so high as observed here. Thus, the PL's model seems unlikely to be the origin. Alternatively, Abrikosov's quantum LMR model shows that

LMR can appear in systems with a gapless linear energy spectrum and all the carriers occupy only the lowest Landau level in an extreme quantum limit [38,39]. However, the carrier density in our system is so high that multiple Landau levels are filled and the quantum limit condition is not satisfied. Although the GLMR cannot be completely explained by the present theoretical mechanisms, we found that the GLMR's magnitude is linearly proportional to the electron mobility as shown in Fig. 4(b). Since the high mobility originates from the TSSs, it is thus a natural conclusion to link the GLMR with the gapless TSSs in PbTe/SnTe as in many other gapless Dirac systems [42–46].

In conclusion, we have systematically investigated the magnetotransport properties of PbTe/SnTe heterostructures. We discover the GLMR phenomena related to the Dirac fermions and strong metallic behavior at low temperatures in PbTe/SnTe heterostructures with sharp PbTe/SnTe interfaces. By decreasing the carrier density in the PbTe/SnTe heterostructures, the cubic-rhombohedral structural phase transition is exhibited in $R_s(T)$ and 2D WAL occurs in transport. Such a remarkable transport difference might be attributed to the mirror symmetry breaking and increased disorder effect from the lattice distortion in SnTe. The controllable transport in the PbTe/SnTe heterostructure is very significant to the fundamental research in topological matter, magnetoelectronics, and spintronics.

This work was supported by the Natural Science Foundation of China (NSFC) (Grants No. 51571195, No. 51331006, and No. 51590883). We also gratefully acknowledge support from the National Key R&D Program of China (No. 2017YFA0206301). C.W.L. and X.P.A.G. thank NSF (Grant No. DMR-1607631) for supporting the work at CWRU. We thank Wan-rong Geng for kind help in TEM sample preparation.

F.W. and C.-W.L. contributed equally to this work.

[1] Y. Tanaka, Z. Ren, T. Sato, K. Nakayama, S. Souma, T. Takabayashi, K. Segawa, and Y. Ando, Nat. Phys. **8**, 800 (2012).
[2] T. H. Hsieh, H. Lin, J. W. Liu, W. H. Duan, A. Bansil, and L. Fu, Nat. Commun. **3**, 982 (2012).
[3] L. Fu, Phys. Rev. Lett. **106**, 106802 (2011).
[4] P. Dziawa, B. J. Kowalski, K. Dybko, R. Buczko, A. Szczerbakow, M. Szot, E. Łusakowska, T. Balasubramanian, B. M. Wojek, M. H. Berntsen, O. Tjernberg, and T. Story, Nat. Mater. **11**, 1023 (2012).
[5] M. Z. Hasan and C. L. Kane, Rev. Mod. Phys. **82**, 3045 (2010).
[6] X. L. Qi and S. C. Zhang, Rev. Mod. Phys. **83**, 1057 (2011).
[7] L. Fu and C. L. Kane, Phys. Rev. B **76**, 045302 (2007).
[8] X. Qi and S. C. Zhang, Phys. Today **63**(1), 33 (2010).
[9] H. Zhang, C. X. Liu, X.-L. Qi, X. Dai, Z. Fang, and S.-C. Zhang, Nat. Phys. **5**, 438 (2009).
[10] A. A. Burkov and L. Balents, Phys. Rev. Lett. **107**, 127205 (2011).
[11] J. Kim, J. Kim, K.-S. Kim, and S. H. Jhi, Phys. Rev. Lett. **109**, 146601 (2012).
[12] S. A. Owerre, J. Phys.: Condens. Matter **28**, 235501 (2016).
[13] Y. Okada, M. Serbyn, H. Lin, D. Walkup, W. Zhou, C. Dhital, M. Neupane, S. Xu, Y. J. Wang, R. Sankar, F. Chou, A. Bansil, M. Zahid Hasan, S. D. Wilson, L. Fu, and V. Madhavan, Science **341**, 1496 (2013).
[14] M. Serbyn and L. Fu, Phys. Rev. B **90**, 035402 (2014).
[15] E. Tang and L. Fu, Nat. Phys. **10**, 964 (2014).
[16] C. Fang, M. J. Gilbert, and B. A. Bernevig, Phys. Rev. Lett. **112**, 046801 (2014).
[17] Q. Wang, F. Wang, J. Li, Z. Wang, X. Zhan, and J. He, Small **11**, 4613 (2015).
[18] B. A. Assaf, F. Katmis, P. Wei, B. Satpati, Z. Zhang, S. P. Bennett, V. G. Harris, J. S. Moodera, and D. Heiman, Appl. Phys. Lett. **105**, 102108 (2014).
[19] R. Akiyama, K. Fujisawa, T. Yamaguchi, R. Ishikawa, and S. Kuroda, Nano Res. **9**, 490 (2016).
[20] A. A. Taskin, F. Yang, S. Sasaki, K. Segawa, and Y. Ando, Phys. Rev. B **89**, 121302 (2014).
[21] M. Safdar, Q. S. Wang, M. Mirza, Z. X. Wang, K. Xu, and J. He, Nano Lett. **13**, 5344 (2013).
[22] J. Shen, Y. Xie, and J. J. Cha, Nano Lett. **15**, 3827 (2015).
[23] I. Zeljkovic, Y. Okada, M. Serbyn, R. Sankar, D. Walkup, W. Zhou, J. Liu, G. Chang, Y. J. Wang, M. Z. Hasan, F. Chou, H. Lin, A. Bansil, L. Fu, and V. Madhavan, Nat. Mater. **14**, 318 (2015).
[24] B. M. Wojek, M. H. Berntsen, V. Jonsson, A. Szczerbakow, P. Dziawa, B. J. Kowalski, T. Story, and O. Tjernberg, Nat. Commu. **6**, 8463 (2015).
[25] P. S. Mandal, G. Springholz, V. V. Volobuev, O. Caha, A. Varykhalov, E. Golias, G. Bauer, O. Rader, and J. Sánchez-Barriga, Nat. Commun. **8**, 968 (2017).
[26] K. L. I. Kobayashi, Y. Kato, Y. Katayama, and K. F. Komatsubara, Phys. Rev. Lett. **37**, 772 (1976).
[27] K. L. I. Kobayashi, Y. Kato, Y. Katayama, and K. F. Komatsubara, Solid State Commun. **17**, 875 (1975).
[28] See Supplemental Material at http://link.aps.org/supplemental/10.1103/PhysRevB.98.161301 for experimental method, structural characterization and transport results analysis.
[29] S. Takaoka and K. Murase, Phys. Rev. B **20**, 2823 (1979).
[30] H. Z. Lu and S.-Q. Shen, Phys. Rev. B **84**, 125138 (2011).
[31] S. Hikami, A. Larkin, and Y. P. Nagaoka, Theor. Phys. **63**, 707 (1980).
[32] N. Bansal, Y. S. Kim, M. Brahlek, E. Edrey, and S. Oh, Phys. Rev. Lett. **109**, 116804 (2012).
[33] A. Ishida, M. Aoki, and H. Fujiyasu, J. Appl. Phys. **58**, 1901 (1985).
[34] S. Takaoka, T. Okumura, K. Murase, A. Ishida, and H. Fujiyasu, Solid State Commun. **58**, 637 (1986).
[35] K. K. Huynh, Y. Tanabe, and K. Tanigaki, Phys. Rev. Lett. **106**, 217004 (2011).
[36] P. Kapitza, Proc. R. Soc. London, Ser. A **119**, 358 (1928).
[37] R. Xu, A. Husmann, T. F. Rosenbaum, M.-L. Saboungi, J. E. Enderby, and P. B. Littlewood, Nature (London) **390**, 57 (1997).
[38] A. A. Abrikosov, Phys. Rev. B **58**, 2788 (1998).
[39] A. A. Abrikosov, Europhys. Lett. **49**, 789 (2000).
[40] M. M. Parish and P. B. Littlewood, Nature (London) **426**, 162 (2003).
[41] M. M. Parish and P. B. Littlewood, Phys. Rev. B **72**, 094417 (2005).

[42] S. Cho and M. S. Fuhrer, Phys. Rev. B **77**, 081402(R) (2008).
[43] H. Tang, D. Liang, R. L. J. Qiu, and X. P. A. Gao, ACS Nano **5**, 7510 (2011).
[44] X. Wang, Y. Du, S. Dou, and C. Zhang, Phys. Rev. Lett. **108**, 266806 (2012).
[45] J. Feng, Y. Pang, D. Wu, Z. Wang, H. Weng, J. Li, X. Dai, Z. Fang, Y. Shi, and L. Lu, Phys. Rev. B **92**, 081306 (2015).
[46] X. C. Pan, Y. Pan, J. Jiang, H. Zuo, H. Liu, X. Chen, Z. Wei, S. Zhang, Z. Wang, X. Wan, Z. Yang, D. Feng, Z. Xia, L. Li, F. Song, B. Wang, Y. Zhang, and G. Wang, Front. Phys. **12**, 127203 (2017).